

Experimental investigation on drag reduction in a turbulent boundary layer with a submerged synthetic jet

Biao-Hui Li(李彪辉), Kang-Jun Wang(王康俊), Yu-Fei Wang(王宇飞), and Nan Jiang(姜楠)
Citation: Chin. Phys. B, 2022, 31 (**2**): 024702. DOI: 10.1088/1674-1056/ac0da6
Journal homepage: http://cpb.iphy.ac.cn; http://iopscience.iop.org/cpb

What follows is a list of articles you may be interested in

Influence of uniform momentum zones on frictional drag within the turbulent boundary layer

Kangjun Wang(王康俊) and Nan Jiang(姜楠)
Chin. Phys. B, 2021, 30 (**3**): 034703. DOI: 10.1088/1674-1056/abc7a6

Effect of high-or low-speed fluctuations on the small-scale bursting events in an active control experiment

Xiao-Tong Cui(崔晓通), Nan Jiang(姜楠), and Zhan-Qi Tang(唐湛棋)
Chin. Phys. B, 2021, 30 (**1**): 014702. DOI: 10.1088/1674-1056/abc7a9

Coherent structures over riblets in turbulent boundary layer studied by combining time-resolved particle image velocimetry (TRPIV), proper orthogonal decomposition (POD), and finite-time Lyapunov exponent (FTLE)

Shan Li(李山), Nan Jiang(姜楠), Shaoqiong Yang(杨绍琼), Yongxiang Huang(黄永祥), Yanhua Wu(吴彦华)
Chin. Phys. B, 2018, 27 (**10**): 104701. DOI: 10.1088/1674-1056/27/10/104701

Active control of wall-bounded turbulence for drag reduction with piezoelectric oscillators

Jian-Xia Bai(白建侠), Nan Jiang(姜楠), Xiao-Bo Zheng(郑小波), Zhan-Qi Tang(唐湛琪), Kang-Jun Wang(王康俊), Xiao-Tong Cui(崔晓通)
Chin. Phys. B, 2018, 27 (**7**): 074701. DOI: 10.1088/1674-1056/27/7/074701

Particle transport behavior in air channel flow with multi-group Lagrangian tracking

Hao Lu(卢浩), Wen-Jun Zhao(赵文君), Hui-Qiang Zhang(张会强), Bing Wang(王兵), Xi-Lin Wang(王希麟)
Chin. Phys. B, 2017, 26 (**1**): 014702. DOI: 10.1088/1674-1056/26/1/014702

Experimental investigation on drag reduction in a turbulent boundary layer with a submerged synthetic jet

Biao-Hui Li(李彪辉)[1], Kang-Jun Wang(王康俊)[1], Yu-Fei Wang(王宇飞)[1], and Nan Jiang(姜楠)[1,2,†]

[1] *Department of Mechanics, School of Mechanical Engineering, Tianjin University, Tianjin* 300350, *China*
[2] *Key Laboratory of Modern Engineering Mechanics, Tianjin* 300350, *China*

(Received 27 April 2021; revised manuscript received 18 June 2021; accepted manuscript online 23 June 2021)

This work investigates the active control of a fully developed turbulent boundary layer by a submerged synthetic jet actuator. The impacts of the control are explored by measuring the streamwise velocities using particle image velocimetry, and reduction of the skin-friction drag is observed in a certain range downstream of the orifice. The coherent structure is defined and extracted using a spatial two-point correlation function, and it is found that the synthetic jet can efficiently reduce the streamwise scale of the coherent structure. Proper orthogonal decomposition analysis reveals that large-scale turbulent kinetic energy is significantly attenuated with the introduction of a synthetic jet. The conditional averaging results show that the induction effect of the prograde vortex on the low-speed fluid in a large-scale fluctuation velocity field is deadened, thereby suppressing the bursting process near the wall.

Keywords: synthetic jet, active control, turbulent boundary layer, drag reduction

PACS: 47.85.lb, 47.85.ld, 47.27.nb, 47.27.De **DOI:** 10.1088/1674-1056/ac0da6

1. Introduction

Despite the extensive amount of work accumulated over the years, turbulent boundary layer (TBL) control for reduction of skin friction is still a significant research topic owing to its great potential benefits.[1,2] Compared with passive control,[3–6] active control has better adaptability to complicated flow and can achieve an optimal control effect with a small energy input.[7–10] Among active control methods, steady blowing,[11] periodic blowing[12] and synthetic jets[13] can suppress the regeneration of the wall structure by weakening the burst of turbulence, thus reducing drag.

Chung *et al.*[14] computed the influence of wall blowing and suction on a fully developed, equilibrium turbulent channel flow through direct numerical simulation; they found that blowing makes the near-wall flow more isotropic. In contrast, under suction conditions, the anisotropy in the near-wall region is notably reinforced. Park *et al.*[15] experimentally probed the impact of periodic blowing and suction on the TBL using particle image velocimetry (PIV). Their results demonstrated that velocity retardation at the near-wall can bring about a decrease in skin friction under the action of blowing, and the attenuation of wall friction resistance was enhanced with increasing forcing frequency.

In recent years, the development of synthetic jet actuators (SJAs) has provided a novel means of applying drag reduction control for TBLs,[16,17] most importantly because they can impart extra momentum into the control region while injecting zero mass.[18,19] Adel Abbas *et al.*[20] summarized the state of the art of several technologies oriented to active control for turbulent drag reduction and pointed out that a SJA is one of the most crucial control modes. Guo *et al.*[21] introduced a local high-frequency perturbation to a flat-plate TBL with a synthetic jet; the disturbance gradually developed downstream of the slot and ultimately affected the near-wall regeneration mechanism of the turbulent structures. Ye *et al.*[22] adopted a synthetic jet array to modify the flow field structure in a TBL. Once the array was turned on, the near-wall structure was elevated, which thickened the viscous sublayer and reduced frictional resistance.

Previous studies have proved the feasibility and enormous potential of synthetic jets for the reduction of TBL drag; however, most of the relevant research has been carried out in wind tunnels.[23,24] Considering the current urgent need for underwater drag reduction control, we employed an active control scheme with a submerged SJA to disturb the flow field. Time-resolved particle image velocimetry (TR-PIV) was used to obtain quantitative measurements. The single-pixel ensemble correlation (SPEC) algorithm was utilized to accurately measure the velocity in the near-wall region to overcome the limitations of traditional PIV in calculating wall friction velocity.[25] Based on an assessment of the spatial characteristics of fluctuation velocity, the scale features of the flow were separated by proper orthogonal decomposition (POD); finally, conditional averaging was used to further reveal the influence of the synthetic jet.

2. Experimental setup and procedure

The experiments were carried out in a low-speed recirculating water channel at Tianjin University, as shown in Fig. 1(a). The size of the working section was 6200 mm ×

†Corresponding author. E-mail: nanj@tju.edu.cn
© 2022 Chinese Physical Society and IOP Publishing Ltd

300 mm × 380 mm (length × width × height) and the background turbulence intensity was estimated to be about 1.5%. A zero-pressure gradient boundary layer flow was developed along a smooth Plexiglas plate with dimensions of 2900 mm × 294 mm × 20 mm (length × width × thickness) and a 4:1 elliptical leading edge. The fully developed TBL was stimulated by a trip wire with a diameter of 2 mm at the plate 100 mm downstream of the leading edge. On the central line 2450 mm away from the leading edge of the plate, a 1-mm long and 10-mm wide hole was made in the test plate where the actuator was situated underneath to generate the synthetic jet, as illustrated in Fig. 1(b). The signal of the SJA had a sinusoidal waveform with a voltage of 9 V, and an excitation frequency of 26 Hz. The coordinate axes x, y, and z denote the streamwise, wall-normal, and spanwise directions, respectively, while the corresponding velocities are designated as u, v, and w. The center of the outlet of the synthetic jet in the streamwise direction is defined as $x = 0$.

The TR-PIV system was used to measure the instantaneous velocity field. The fluid was seeded with polyamide particles with a mean diameter of 20 μm and a specific gravity of 1.03 g/cm^3.The measurement plane (x–y plane) was illuminated by a laser sheet with a light thickness of around 1mm. The investigations were conducted in two parts, including experiments on the characteristics of the synthetic jet and experiments on the interaction between the synthetic jet and the mainstream. When there was no flow, 8216 continuous snapshots of particle images were captured by camera #1 (which faced the center of the jet outlet) with a sampling frequency of 400 Hz; these were analyzed by adaptive correlation with interrogation windows of 32 pixels × 32 pixels and an overlap rate of 75%. The field of view was nearly 60.21 mm × 37.63 mm and the spatial distance per vector was 0.3763 mm. Once the inverter motor of the water channel had been activated and until the incoming flow stabilized, two CCD cameras with a resolution of 1280 pixels × 800 pixels recorded 8216 × 4 images separately at the same time. For camera #1, Dynamic Studio software from Dance was utilized to remove noise and transform the particle images to the velocity field. The interrogation window for adaptive correlation was 32 pixels × 32 pixels with a 75% overlap. Eventually, 156 × 92 velocity vectors were reconstructed for each image with a vector pitch of 0.6248 mm. The pseudovector produced by the experimental data was below 1%. For camera #2, the measurement area was approximately 20 mm–50 mm downstream of the synthetic jet exit and the field of view was smaller (with the intention of achieving a higher resolution in the near-wall area and accurately calculating the skin friction velocity by means of SPEC).[26,27] The relative error of the skin friction velocity depends on the ensemble size of the image samples, and the relative error will be less than 0.1% when the ensemble size exceeds 2000.[27] Detailed experimental parameters are included in Table 1.

Table 1. Experimental parameters.

Free-stream velocity	0.23 m/s
Sampling frequency	600 Hz
Number of snapshots	32860
Large field	99.97 mm × 62.48 mm
Scale factor (large field)	0.0781 mm/pixel
Small field	26.72 mm × 16.7 mm
Scale factor (small field)	0.0209 mm/pixel

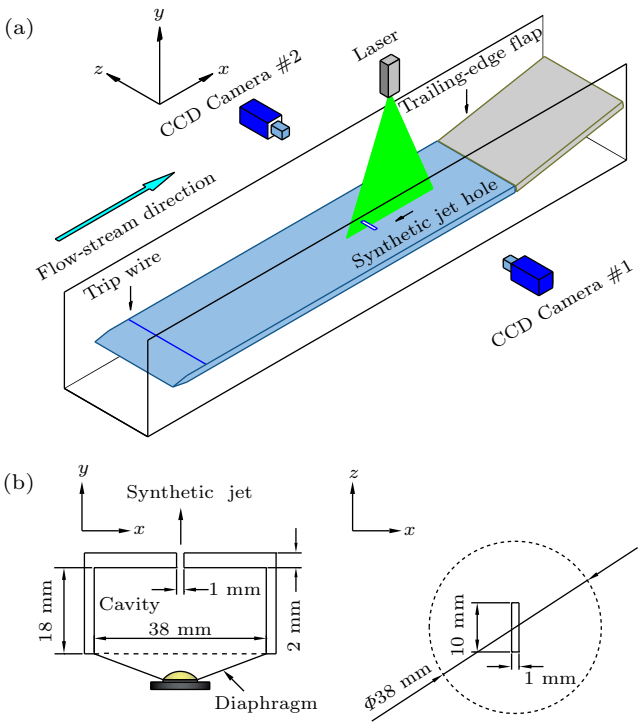


Fig. 1. Schematic diagram of the experimental setup: (a) the test platform; (b) the synthetic jet actuator.

3. Result and analysis

3.1. Characteristics of the synthetic jet

Figure 2(a) plots the time-averaged flow field of the synthetic jet. The coordinates have been normalized by the width of the jet opening d. Although the working process of the synthetic jet is divided into blowing and suction phases,[28] the periodic disturbance of the SJA exerts a similar impression to that of continuous blowing. The directionality of the flow field is single and stable, with only partial backflow near both sides of the exit. Therefore, it is concluded that the impact of the blowing phase on the external environment is greater than that of the suction phase. Meanwhile, the jet is mainly concentrated in the near field and has little effect on the far field. The synthetic jet centerline velocity is given in Fig. 2(b). The maximum velocity appears at about $y/d = 2.4$, after which it decays rapidly and then slowly as y/d increases. The above properties of the synthetic jet signify that it can be implemented in drag reduction control in a TBL.[29]

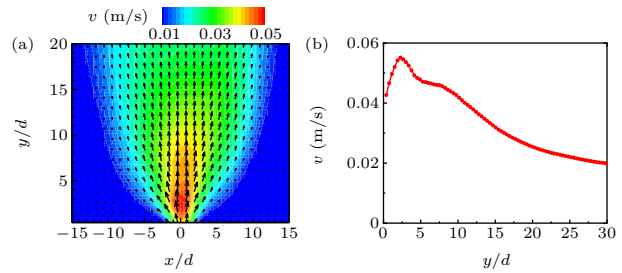


Fig. 2. Characteristics of synthetic jet: (a) time-averaged flow field; (b) synthetic jet centerline velocity.

3.2. Turbulence statistics

Figure 3 compares the contours of the streamwise mean velocity field under different working conditions. When the fluid in the near-wall region flows over the jet outlet, a tiny bulge appears and the thickness of the downstream near-wall region increases while the velocity gradient decreases, leading to a reduction in skin-friction drag. In addition, the rise of the near-wall region caused by the synthetic jet reaches a maximum at 40 mm downstream of the exit, and then gradually reduces. It is estimated that the fluid field will eventually return to the state before the control was applied.

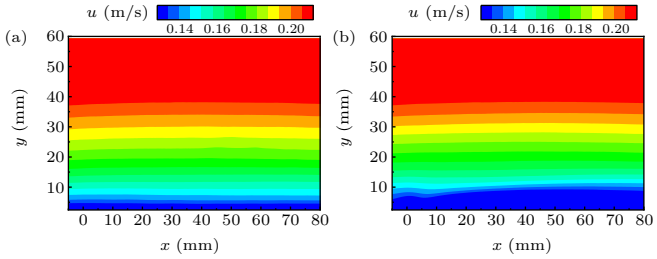


Fig. 3. Contours of the streamwise mean velocity field: (a) 0 V, 0 Hz; (b) 9 V, 26 Hz.

The basic flow parameters in the TBL in the different experiments are summarized in Table 2. U_∞ represents the main stream velocity, δ is the thickness of the TBL and $Re_\tau = u_\tau\delta/\nu$ and $Re_\theta = U_\infty\theta/\nu$ are Reynolds numbers based on the skin friction velocity u_τ and momentum thickness θ, respectively.

As indicated in Fig. 4(a), the outer-scale average velocity profiles of the viscous sublayer show good linear distribution and can be linearly fitted.[30] The wall shear stress τ_w can be computed from the profile slope according to

$$\tau_w = \rho\nu\partial u/\partial y. \tag{1}$$

Here, the density of water ρ is 998 kg/m^3 and the kinematic viscosity ν is 9.7×10^{-7} m^2/s. The skin friction velocity u_τ will be obtained by the function

$$\tau_w = \rho u_\tau^2. \tag{2}$$

Then, the fictional factor is defined as follows:

$$C_f = 2\tau_w/\rho U_\infty^2 = 2u_\tau^2/U_\infty^2, \tag{3}$$

so the drag reduction ratio DR can be expressed as

$$\mathrm{DR} = (1 - C_{f1}/C_{f0})\times 100\%, \tag{4}$$

where C_{f0} and C_{f1} denote the frictional coefficients before and after control is applied, respectively. As a result, the average percentage drag reduction 20 mm–50 mm downstream of the jet opening is 19.37%.

Table 2. Turbulent boundary layer properties for each condition.

Case	U_∞ (m/s)	δ (mm)	u_τ (m/s)	Re_τ	Re_θ	C_f (10^{-3})	DR (%)
0 V, 0 Hz	0.2278	50.54	0.00920	479.3	1451.8	3.263	–
9 V, 26 Hz	0.2286	49.92	0.00829	426.6	1495.0	2.631	19.37

In Fig. 4(b), the mean velocity profiles are normalized by inner-scale units $u^+ = u/u_\tau$, $y^+ = yu_\tau/\nu$. Overall, the log-law region has lifted up clearly in the presence of the synthetic jet, which is a typical feature of drag reduction in a TBL.[31,32]

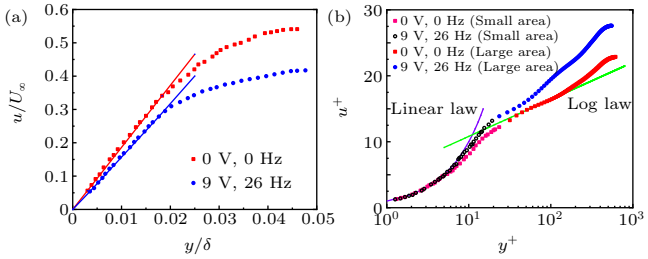


Fig. 4. Mean velocity profiles: (a) outer-scale; (b) inner-scale.

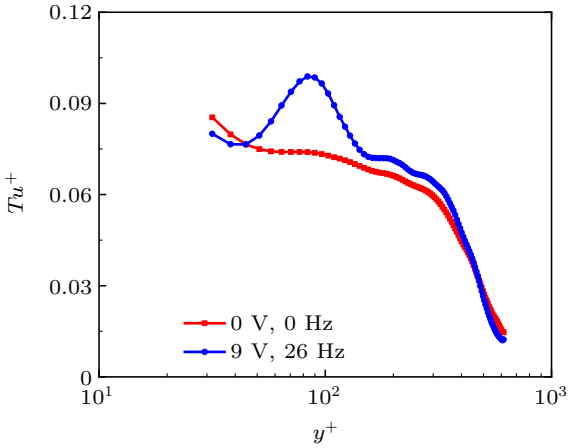


Fig. 5. Comparison of streamwise turbulence intensity.

Figure 5 shows the contrasting profiles of streamwise turbulence intensity Tu^+ ($Tu^+ = u'_{rms}/U_\infty$, u'_{rms} is the root mean square of streamwise fluctuating velocity u'). In the near-wall region of $y^+ < 45$, the controlled Tu^+ is less than the uncontrolled value; this is caused by the uplift of the streamwise vortices under the effect of upwash restraining the interaction between the coherent structure and the wall. The controlled peak appears near $y^+ = 85$. This dual-peak phenomenon has been corroborated by previous studies.[29,33] Additionally, in the process of moving along the streamwise and the wall-normal direction, the spanwise vortex generated by the synthetic jet

continuously interacts with the surrounding fluid resulting in a large turbulence intensity, and the peak in the Tu^+ profile can be considered as the center of the spanwise vortex.[29] After the peak, the synthetic jet gradually loses its influence on the flow field, and Tu^+ finally shows a similar trend to the uncontrolled case.

3.3. Two-point correlation

Spatial two-point correlation involves a great deal of information regarding the average spatial structure in wall turbulence;[34,35] therefore, the impact of a synthetic jet on the underlying structure of the flow can be quantitatively explored by this method. The two-point velocity correlation coefficients are given by

$$R_{ij}(\Delta x, y; y_{\rm ref}) = \frac{\left\langle u_i'(x, y_{\rm ref}) u_j'(x+\Delta x, y)\right\rangle}{\sigma_i(y_{\rm ref})\sigma_j(y)}, \tag{5}$$

where Δx is the spatial distance between two correlated points in the streamwise direction, σ_i and σ_j are root-mean squares of the i-th and j-th velocity components and $y_{\rm ref}$ signifies the reference wall-normal position. In this study, $y_{\rm ref} = 0.15\delta$, which is close to the location of the peak Tu^+ mentioned above.

Figures 6(a) and 6(b) present contours of $R_{\rm uu}$ for different cases. There is a certain similarity between the $R_{\rm uu}$ as the streamwise scale is larger than the wall-normal scale. The difference is that the controlled $R_{\rm uu}$ is farther away from the wall. Moreover, the inclination angle of $R_{\rm uu}$, related to the average inclination of the hairpin packet, is distinctly greater in the controlled case. To quantify the angle, we used the least-squares method[36] to fit the boundary points on the contours. Considering the regularity of the ellipse fitting, the reference value of the contour level was determined as 0.3. The inclination angles before and after control is utilized are 6.4° and 9.3°, respectively, suggesting that the vortex organization is greatly lifted under the action of the synthetic jet.

Quantitative characterization of the one-dimensional profiles of $R_{\rm uu}$ is displayed in Fig. 6(c). Evidently, the presence of a synthetic jet shortens the streamwise extent $Lx_{\rm uu}$, which is defined as twice the streamwise distance between the correlation level of 0.5 and the self-correlation peak.[5] $Lx_{\rm uu}$ is about 20% smaller for the controlled case, and it can be concluded that the synthetic jet has an inhibitory effect on the streamwise scale of $R_{\rm uu}$.

Figures 7(a) and 7(b) give the contours of $R_{\rm vv}$ for different cases. Compared with $R_{\rm uu}$, $R_{\rm vv}$ is considerably less elongated in the streamwise direction. With respect to the uncontrolled case, the contour of $R_{\rm vv}$ is slightly inclined to the upper right, while with the action of the SJA it is more perpendicular to the wall and flatter in outline, which can be regarded as the modulation in impact produced by the synthetic jet in the wall-normal direction during the blowing phase.

A quantitative contrast of the one-dimensional profiles of $R_{\rm vv}$ is presented in Fig. 7(c). The streamwise extent $Lx_{\rm vv}$ has the same definition as $Lx_{\rm uu}$. At a correlation level of 0.5, $Lx_{\rm vv}$ is around 13% lower than in the case without control, indicating that the synthetic jet also blocks the extension of $R_{\rm vv}$ in the streamwise direction.

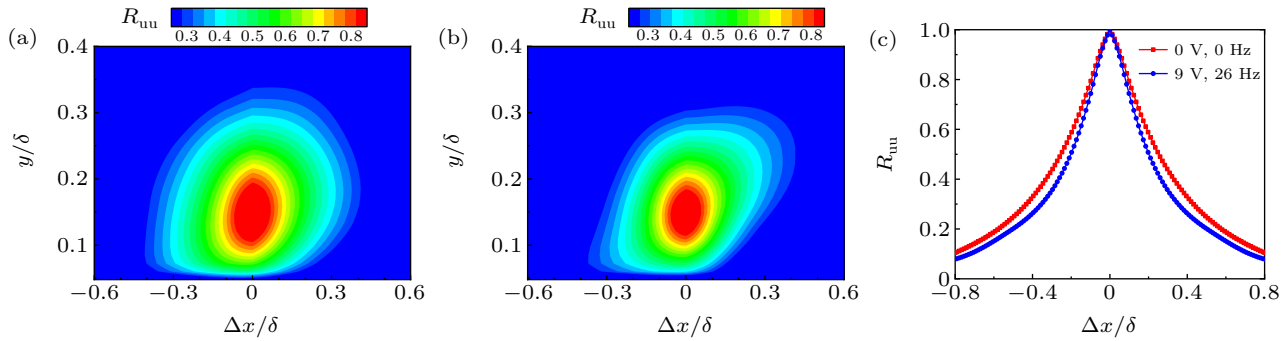


Fig. 6. Contours of spatial two-point correlation coefficients $R_{\rm uu}$ and one-dimensional profiles: (a) 0 V, 0 Hz; (b) 9 V, 26 Hz. (c) Streamwise extents.

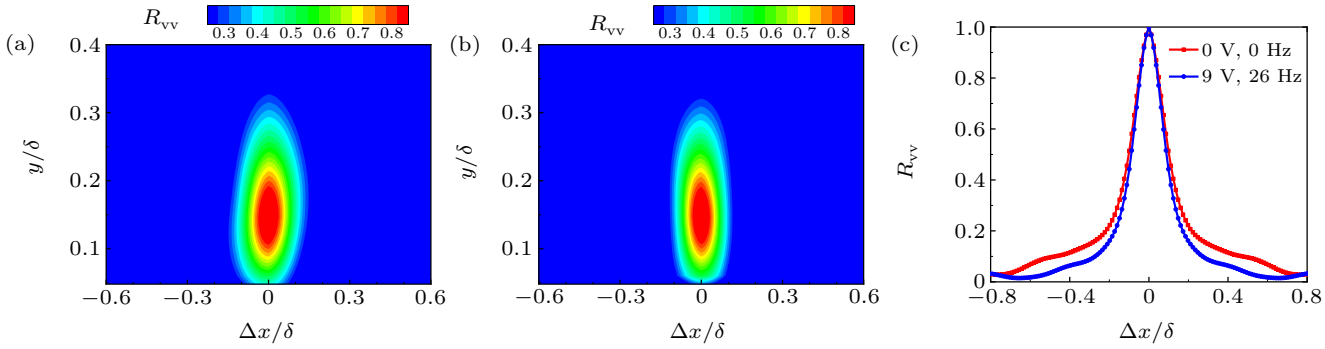


Fig. 7. Contours of spatial two-point correlation coefficients $R_{\rm vv}$ and one-dimensional profiles: (a) 0 V, 0 Hz; (b) 9 V, 26 Hz. (c) Streamwise extents.

3.4. Proper orthogonal decomposition analysis

As described in Subsection 3.3, it seems that the current synthetic jet has modified the streamwise coherence of both R_{uu} and R_{vv}. Snapshot POD could be employed from the perspective of turbulent kinetic energy (TKE)[37,38] for the purpose of separating the scale features of flow. The specific process is as follows.

First, the fluctuating velocity field matrix is written as

$$M = [m^1 m^2 m^3 \cdots m^{N-1} m^N], \quad N = 8215. \tag{6}$$

Here, $m = (u', v')$ and each column of the matrix corresponds to a moment and contains the two-component information about the fluctuating velocity at all spatial velocity measurement points. Then the spatial correlation matrix can be obtained as

$$R = M^{\mathrm{T}} M, \tag{7}$$

where M^{T} is the transposed matrix of M. Afterwards, we solve the eigenvalues and eigenvectors of R

$$RA^i = \lambda_i A^i, \tag{8}$$

where A^i is the eigenvector and the eigenvalue λ_i represents the TKE contribution of the i-th POD mode.

The basic function for the POD mode is expressed as

$$\phi_i = \frac{\sum_{n=1}^{N} A_i^n m^n}{\left\| \sum_{n=1}^{N} A_i^n m^n \right\|}, \quad (i = 1, 2, 3, \ldots, N-1, N). \tag{9}$$

After the above calculation process, the POD mode can be realized as

$$m(x, t_n) = \sum_{n=1}^{N} a_n(t) \phi_n(x). \tag{10}$$

Here, the random temporal function $a_n = \phi^{\mathrm{T}} m_n$.

Figure 8(a) refers to the fractional contributions of single POD modes to total TKE. For the first four modes, the proportion of energy after control is lower than with no control. Starting with the fifth mode, the result is reversed. That is to say, the application of the synthetic jet causes the low-order (large-scale) energy to be weakened while enhancing the high-order (small-scale) energetic turbulent events. Figure 8(b) displays the distribution of cumulative energy. In the low-order mode range, the cumulative energy of the controlled flow field is obviously smaller than that of the uncontrolled field, whereas the two curves are relatively close from the 200th order on, showing that the more coherent small-scale structures are concentrated in the flow field when the synthetic jet exists.

The contours for the first-order POD mode in both conditions are shown in Fig. 9. Since the POD is realized based on a statistical correlation function, the first-order mode can be seen as the average result of flow field pulsation. The contours have a similar distribution to the coherent structure acquired by spatial correlation. The controlled flow field is constantly regulated by the synthetic jet, which impedes the growth of a coherent structure in the flow direction and lifts the coherent structure away from the wall, thereby weakening the interaction between the coherent structure and the wall as the flow moves downstream.

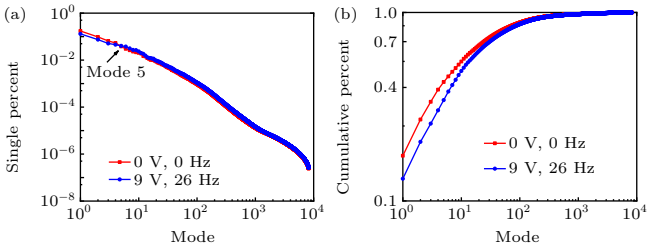


Fig. 8. POD spectrum energy distributions: (a) single energy distribution; (b) cumulative energy distribution.

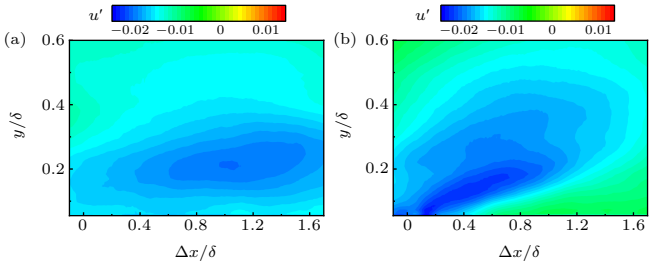


Fig. 9. Contours for the first-order POD mode: (a) 0 V, 0 Hz; (b) 9 V, 26 Hz.

In general, the snapshot POD not only separates the coherent structures at different scales according to their contribution to the TKE, but also reconstructs low-dimensional dynamic systems and cuts down the complexity of turbulence.

A low-order reconstruction of the leading K POD modes is taken to be

$$m_{\mathrm{L}}(x, t_n) = \sum_{k=1}^{K} a_k(t_n) \phi_k(x). \tag{11}$$

Consequently, the residual field, composed of the high-order modes, is given by

$$m_{\mathrm{R}}(x, t_n) = \sum_{k=K+1}^{N} a_k(t_n) \phi_k(x) = m(x, t_n) - m_{\mathrm{L}}(x, t_n). \tag{12}$$

In this paper, the number of modes selected for reconstruction is the minimum number required to capture 80% of the TKE in the measurement area. Figure 10 displays the profiles of Tu^+ calculated from low-order (large-scale) and associated residual (small-scale) velocity fields. As can be seen from this figure, the trends of large-scale $y^+ = 45$ and small-scale contribution to Tu^+ are similar to the results of Wu and Christensen[39] in the case of no control. In Fig. 10(a), the curve of large-scale Tu^+ is consistent with Fig. 5, whereas the corresponding amplitudes decrease. Furthermore, the restraint of the synthetic jet on large-scale Tu^+ can reach $y^+ = 60$, higher than that in Fig. 5, and the peak position of Tu^+ remains unchanged. By comparison, as illustrated in Fig. 10(b), in the near-wall region the suppression on the small-scale Tu^+ by the synthetic

jet is similar to that in Fig. 5, and the peak position of Tu^+ is $y^+ = 65$, closer to the wall; this is due to the small-scale spanwise vortex introduced by the synthetic jet. The above analysis of Figs. 5 and 10 shows that the large-scale components of Tu^+ account for a relatively high proportion, and the synthetic jet shows more effective inhibition of these components.

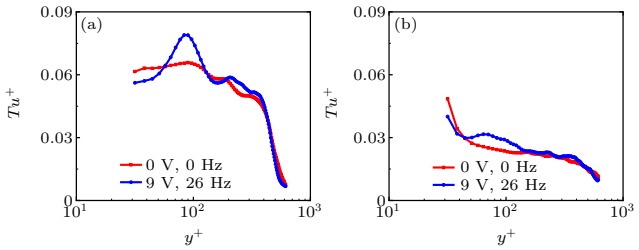


Fig. 10. Comparison of Tu^+ from low-order and residual velocity fields: (a) low-order contribution; (b) residual contribution.

3.5. Conditional average

In order to identify the variation in large- and small-scale turbulent fluctuations and vortex structures the method of conditional averaging was implemented, based on spanwise vorticity as a conditional event. The λ_{ci} criterion[40] was adopted for visualizing vortex structures using the following equation:

$$\Lambda_{ci} = \lambda_{ci}\mathrm{sign}(\omega) = \lambda_{ci}\omega/|\omega|. \tag{13}$$

Here, λ_{ci} stands for the imaginary part of the complex eigenvalue of the velocity gradient tensor and ω is the spanwise vorticity. The specific expression for the detection function is defined as

$$\begin{aligned}\left\langle u'_{\mathrm{L}}(\Delta x,y)\right\rangle &= \left\langle u'_{\mathrm{L}}(x+\Delta x,y)\,|\Lambda_{ci}(x,y_{\mathrm{ref}})<0\right\rangle,\\ \left\langle u'_{\mathrm{S}}(\Delta x,y)\right\rangle &= \left\langle u'_{\mathrm{S}}(x+\Delta x,y)\,|\Lambda_{ci}(x,y_{\mathrm{ref}})<0\right\rangle,\end{aligned} \tag{14}$$

where u'_{L} and u'_{S} are the large and small-scale u', respectively, and $y_{\mathrm{ref}} = 0.15\delta$. Since the coherent structure extracted by conditional detection conforms to the structural characteristics of a hairpin vortex, and $\Lambda_{ci} < 0$, the velocity fields after conditional averaging denote the average of the fluctuating velocities near the head of the hairpin vortex and the ejection event of low-speed fluid.[41]

The contours presented in Fig. 11 are the conditional averages of the large-scale streamwise fluctuating velocity. As shown in Figs. 11(a) and 11(b), there is a strong clockwise rotating vortex in the detection center, and below it are low-speed upward ejected fluids induced by the vortex. The tough shear between the prograde vortex and the wall is the main source of wall frictional resistance.[42] Before and after applying control, the positive fluctuation increases successively, although the negative fluctuation continues to decrease. This is attributed to the presence of the synthetic jet causing the prograde vortex to rise, thus impairing its inductive influence on the low-speed fluid, and the diminution of the induced region in the streamwise range is conducive to weakening the burst

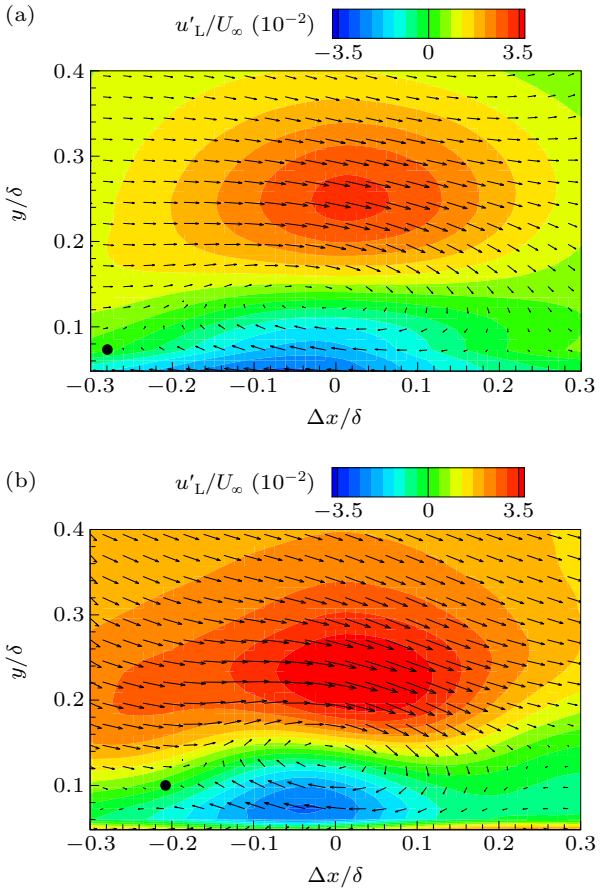


Fig. 11. Conditional average contours of u'_{L}: (a) 0 V, 0 Hz; (b) 9 V, 26 Hz.

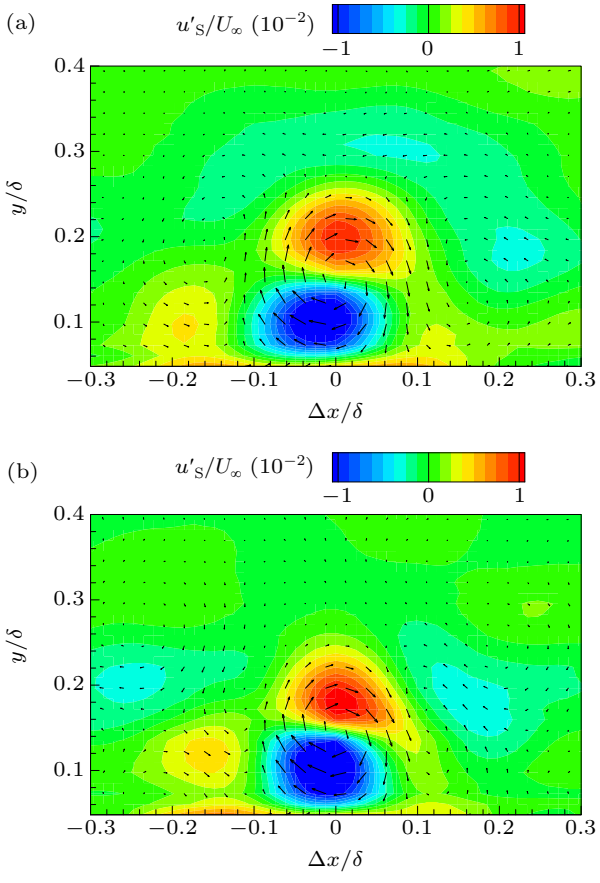


Fig. 12. Conditional average contours of u'_{S}: (a) 0 V, 0 Hz; (b) 9 V, 26 Hz.

intensity of turbulence events in the near-wall. Beyond that, upstream of the vortex, the upward ejection of low-speed fluid fails because of interaction with the high-speed fluid sweeping downward, so that the fluid almost stagnates and forms a stagnation point (black point)[43] where violent Reynolds stress events occur. The regulatory effects of the synthetic jet on the mainstream lead to the stagnation point moving in the direction normal to the far wall, greatly lowering the momentum energy and mass transport ascribed to the Reynolds shear stress at the near wall and realizing the purpose of drag reduction.

The conditional average contours of small-scale streamwise fluctuating velocity are plotted in Fig. 12. For the synthetic jet, the positive and negative small-scale fluctuations both increase slightly, and the position of the prograde vorticity is closer to the wall. The enhancement of small-scale fluctuation includes two aspects: one is that small-scale disturbance incessantly arises from the synthetic jet, and the other is dissipation of the large-scale structure related to wall friction by such a perturbation.

4. Conclusion

The characteristics of a submerged synthetic jet and its influence on the TBL were explored by TR-PIV technology. The following conclusions are presented.

(i) The blowing phase is dominant over the whole jet cycle; this exerts an effect similar to continuous blowing, suitable for active drag reduction control in the TBL.

(ii) In the near-wall region, the synthetic jet raises the streamwise vortices, Tu^+ is attenuated and an average drag reduction rate of 19.37% in the range of 20 mm–50 mm downstream of the opening is achieved.

(iii) Under the impact of upwash, the coherent structure is lifted and extension along the streamwise direction is hindered, resulting in a restraining of the interaction with the wall in the downstream region.

(iv) The synthetic jet significantly attenuates the large-scale TKE related to the skin-friction drag in the flow field, so that the distribution of TKE is concentrated to a small-scale coherent structure.

(v) Introduction of the synthetic jet deadens the induction effect of the prograde vortex on the low-speed fluid in the large-scale fluctuation velocity field, and reduces the burst process of turbulence events near the wall, thus realizing drag reduction.

Acknowledgments

Project supported by the National Natural Science Foundation of China (Grant Nos. 11732010, 11972251, 11872272, 11902218, and 11802195) and the National Key Research and Development Program of China, on 'Green Buildings and Building Industrialization' (Grant No. 2018YFC0705300).

References

[1] Kim J 2003 *Phys. Fluids* **15** 1093
[2] Corke T C and Thomas F O 2018 *AIAA J.* **56** 3835
[3] Wang X L, Di Q F, Zhang R L, Gu C Y and Gong W 2012 *Acta Phys. Sin.* **61** 146801 (in Chinese)
[4] Wang B, Wang J, Chen D, Sun N and Wang T 2017 *Chin. Phys. B* **26** 054701
[5] Cui G, Pan C, Wu D, Ye Q and Wang J 2019 *Chin. J. Aeronaut.* **32** 2433
[6] Li S, Jiang N and Yang S Q 2019 *Acta Phys. Sin.* **68** 074702 (in Chinese)
[7] Zhou Y and Bai H 2011 *Sci. China-Phys. Mech. Astron.* **54** 1289
[8] Han Y, Zhang H, Fan B C, Li J, Jiang D W and Zhao Z J 2017 *Chin. Phys. B* **26** 084704
[9] Jiang D W, Zhang H, Fan B C and Wang A H 2019 *Chin. Phys. B* **28** 054701
[10] Zhang L, Shan X and Xie T 2020 *IEEE Access* **8** 7039
[11] Kametani Y, Fukagata K, Örlü R and Schlatter P 2015 *Int. J. Heat Fluid Flow* **55** 132
[12] Bai H L, Zhou Y, Zhang W G, Xu S J, Wang Y and Antonia R A 2014 *J. Fluid Mech.* **750** 316
[13] Lasagna D, Orazi M and Iuso G 2014 *Fluid Dyn. Res.* **46** 015501
[14] Chung Y M, Sung H J and Krogstad P A 2002 *AIAA J.* **40** 1529
[15] Park Y S, Park S H and Sung H J 2003 *Exp. Fluids* **34** 697
[16] Glezer A and Amitay M 2003 *Annu. Rev. Fluid Mech.* **34** 503
[17] Murugan T, Deyashi M, Dey S, Rana S C and Chatterjee P K 2016 *Def. Sci. J.* **66** 489
[18] Jabbal M and Zhong S 2008 *Int. J. Heat Fluid Flow* **29** 119
[19] Chaudhry I A and Zhong S 2014 *J. Visualization* **17** 101
[20] Abbas A, Bugeda G, Ferrer E, Fu S, Periaux J, Pons-Prats J, Valero E and Zheng Y 2017 *Sci. China: Technol. Sci.* **60** 1281
[21] Guo H, Huang Q M, Liu P Q and Qu Q L 2015 *Fluid Dyn. Res.* **47** 045501
[22] Ye Z, Jiang Y, Zhang Y, Zou J and Zheng Y 2019 *Int. J. Heat Technol.* **37** 893
[23] Berk T, Hutchins N, Marusic I and Ganapathisubramani B 2018 *J. Fluid Mech.* **856** 531
[24] Cannata M, Cafiero G and Iuso G 2020 *AIAA J.* **58** 2042
[25] Westerweel J, Geelhoed P F and Lindken R 2004 *Exp. Fluids* **37** 375
[26] Kähler C J, Scharnowski S and Cierpka C 2012 *Exp. Fluids* **52** 1629
[27] Shen J, Pan C and Wang J 2014 *Sci. China-Phys. Mech. Astron.* **57** 1352
[28] Smith B L and Smith A 1998 *Phys. Fluids* **10** 2281
[29] Lu L, Li D, Gao Z, Cao Z, Bai Y and Zheng J 2020 *Acta Mech. Sin.* **36** 1171
[30] Cui X, Jiang N, Zheng X and Tang Z 2019 *Acta Mech. Sin.* **36** 12
[31] Tian H, Zhang J, Jiang N and Yao Z 2015 *Exp. Therm. Fluid Sci.* **69** 27
[32] Bai J X, Jiang N, Zheng X B, Tang Z Q, Wang K J and Cui X T 2018 *Chin. Phys. B* **27** 074701
[33] Park S H, Lee I and Sung H J 2001 *Exp. Fluids* **31** 384
[34] Ganapathisubramani B, Hutchins N, Hambleton W T, Longmire E K and Marusic I 2005 *J. Fluid Mech.* **524** 57
[35] Hong J, Katz J and Schultz M P 2011 *J. Fluid Mech.* **667** 1
[36] Volino R J, Schultz M P and Flack K A 2007 *J. Fluid Mech.* **592** 263
[37] Geers L F G, Tummers M J and Hanjalić K 2005 *Phys. Fluids* **17** 055105
[38] Kostas J, Soria J and Chong M S 2005 *Exp. Fluids* **38** 146
[39] Wu Y and Christensen K T 2010 *J. Fluid Mech.* **655** 380
[40] Zhou J, Adrian R J, Balachandar S and Kendall T M 1999 *J. Fluid Mech.* **387** 353
[41] Adrian R, Meinhart C and Tomkins C 2000 *J. Fluid Mech.* **422** 1
[42] Fukagata K, Iwamoto K and Kasagi N 2002 *Phys. Fluids* **14** L73
[43] Yang S Q and Jiang N 2012 *Sci. China: Phys. Mech. Astron.* **55** 1863